Velocity statistics in turbulent channel flow up to $Re_\tau = 4000$

MATTEO BERNARDINI, SERGIO PIROZZOLI and PAOLO ORLANDI

Dipartimento di Ingegneria Meccanica e Aerospaziale, Università di Roma 'La Sapienza'
Via Eudossiana 18, 00184 Roma, Italy

The high-Reynolds-number behavior of the canonical incompressible turbulent channel flow is investigated through large-scale direct numerical simulation (DNS). A Reynolds number is achieved ($Re_\tau = h/\delta_v \approx 4000$, where h is the channel half-height, and δ_v is the viscous length scale) at which theory predicts the onset of phenomena typical of the asymptotic Reynolds number regime, namely a sensible layer with logarithmic variation of the mean velocity profile, and Kolmogorov scaling of the velocity spectra. Although higher Reynolds numbers can be achieved in experiments, the main advantage of the present DNS study is access to the full three-dimensional flow field. Consistent with refined overlap arguments (Afzal & Yajnik 1973; Jiménez & Moser 2007), our results suggest that the mean velocity profile never achieves a truly logarithmic profile, and the logarithmic diagnostic function instead exhibits a linear variation in the outer layer whose slope decreases with the Reynolds number. The extrapolated value of the von Karman constant is $k \approx 0.41$. A near logarithmic layer is observed in the spanwise velocity variance, as predicted by Townsend's attached eddy hypothesis, whereas the streamwise variance seems to exhibit a plateau, perhaps being still affected by low-Reynolds-number effects. Comparison with previous DNS data at lower Reynolds number suggests enhancement of the imprinting effect of outer-layer eddies onto the near-wall region. This mechanisms is associated with excess turbulence kinetic energy production in the outer layer, and it reflects in flow visualizations and in the streamwise velocity spectra, which exhibit sharp peaks in the outer layer. Associated with the outer energy production site, we find evidence of a Kolmogorov-like inertial range, limited to the spanwise spectral density of u, whereas power laws with different exponents are found for the other spectra. Finally, arguments are given to explain the 'odd' scaling of the streamwise velocity variances, based on the analysis of the kinetic energy production term.

1. Introduction

The study of turbulent flows over solid surfaces has a great importance in engineering fluid dynamics, but it is also a subject of great intrinsic academic interest. According to the common notion, turbulence in the near-wall layer is approximately universal, when quantities are scaled in wall units (namely, the friction velocity $u_\tau = \sqrt{\tau_w/\rho}$, and the viscous length-scale $\delta_v = \nu/u_\tau$). On the other hand, far from the wall, the correct length scale is the thickness of the wall layer (in channels, the half-width h), whereas the relevant velocity scale is still u_τ. Conventionally (Pope 2000), the inner layer is assumed to end at $y/h \approx 0.1$ and the outer layer to start at $y^+ \approx 50$. Matching the mean velocity profile between in the overlap region between the inner and the outer layer (if any) yields the

logarithmic law, which then only emerges if the friction Reynolds number, $Re_\tau = h/\delta_v$ is of the order of thousands, or so. The universal nature of wall turbulence has been put into question by a series of studies which have highlighted a series of violations of the universal structure, the most evident being perhaps the variation of the near-wall peak of the streamwise turbulence intensity, whose amplitude is found to grow logarithmically with the friction Reynolds number (Klewicki & Falco 1990; DeGraaff & Eaton 2000; Marusic & Kunkel 2010). This behavior has been linked to the influence of outer-scaled eddies, which mainly contain wall-parallel, inactive motions (Kim & Adrian 1999; Guala *et al.* 2006; Hutchins & Marusic 2007). The imprint of the outer-layer eddies becomes more evident as Re_τ is increased, eventually leading to violation of the pure wall scaling. Is is generally believed that, to be able to probe high-Reynolds-number effects, friction Reynolds numbers of the order of a few thousands should be explored, the consensus threshold to observe an order-of-magnitude logarithmic variation of the mean velocity being $Re_\tau \approx 4000$ (Jiménez & Moser 2007; Hutchins & Marusic 2007).

Studying wall-bounded turbulent flows (boundary layers, channels, pipes) in the moderate-to-high Reynolds-number regime is then a challenging task both for experiments, because of the stringent requirements on the velocity probe size (Hultmark *et al.* 2010), and even more for DNS. The latter offer the advantage of easier access to the full three-dimensional flow fields, but it is seriously hampered by the need of huge computational resources. Given the approximate proportionality between the Kolmogorov scale and the viscous length scale at the wall (Pope 2000), it is found that the energetically relevant scales of motion are resolved (at least in pseudo-spectral calculations) provided the spacings in the wall-parallel directions are $\Delta x^+ \approx 10$, $\Delta z^+ \approx 6$ (the superscript + is hereafter used to denote quantities made nondimensional with u_τ and δ_v). Further, to keep the resolution constant in terms of Kolmogorov units, the number of collocation points in the wall-normal direction shall grow as $Re_\tau^{3/4}$ (Pope 2000), hence making up for a total number of points growing as $Re_\tau^{11/4}$. This restriction makes the numerical simulation of wall-bounded flows at high Reynolds number (in the operational sense given above) quite challenging. To date, the highest Reynolds number attained in incompressible boundary layer DNS is $Re_\tau \approx 2000$ (Sillero *et al.* 2013), for channel flows $Re_\tau \approx 2000$ (Hoyas & Jiménez 2006), and for pipe flows $Re_\tau \approx 1100$ (Wu & Moin 2008). $Re_\tau \approx 4000$ was recently achieved in a compressible boundary layer DNS, by the present authors (Pirozzoli & Bernardini 2013).

In this paper we present novel data from incompressible channel flow DNS, which extends the Reynolds number envelope of numerical channels to $Re_\tau \approx 4000$, thus meeting the constraints for the flow to be regarded at least representative of the high-Reynolds-number regime. The numerical methodology used for the purpose is explained in §2, and the flow statistics are presented in §3, which includes a discussion of the results. Final comments are given in §4.

2. Computational setup

We solve the Navier-Stokes equations for a divergence-free velocity field, by enforcing a time-varying pressure gradient to maintain a constant mass flow rate. The equations are discretized in an orthogonal coordinate system (x, y, z denote the streamwise, wall-normal and spanwise directions) using staggered central second-order finite-difference approximations, which guarantee that kinetic energy is globally conserved in the limit of inviscid flow. Time advancement is achieved by a hybrid third-order low-storage Runge-Kutta algorithm (Bernardini & Pirozzoli 2009) coupled with the second-order Crank-Nicolson scheme, combined in the fractional-step procedure, whereby the convective and

Flow case	Line style	Re_b	Re_τ	N_x	N_y	N_z	Δx^+	Δz^+	Tu_τ/h
CH1	Dashed	20063	550	1024	256	512	10.0	6.7	36.3
CH2	Dash-dot	39600	999	2048	384	1024	9.2	6.1	26.9
CH3	Dash-dot-dot	87067	2022	4096	768	2048	9.3	6.2	14.9
CH4	Solid	191333	4079	8192	1024	4096	9.4	6.2	8.54

Table 1: List of parameters for turbulent channel flow cases. $Re_b = 2hu_b/\nu$ is the bulk Reynolds number, and $Re_\tau = hu_\tau/\nu$ is the friction Reynolds number. N_x, N_y, N_z are the number of grid points in the streamwise, wall-normal, and spanwise directions. Δx^+, Δz^+ are the grid spacings in the wall-parallel direction, in wall units. The simulation time T is given in terms of eddy turnover times h/u_τ.

diffusive terms are treated explicitly and implicitly, respectively. The Poisson equation for the pressure field, stemming from the incompressibility condition, is efficiently solved using a direct solver based on Fourier transform methods, as described by Kim & Moin (1985). A full description of the numerical method is provided in Orlandi (2000).

It is worth noting that the computations are performed in a convective reference frame for which the bulk velocity is zero, i.e. in which the net streamwise mass flux is zero. In addition to allowing a larger computational time-step, this expedient minimizes the dispersion errors associated with the finite-difference discretization, leading to results that are much closer to those of spectral methods (Bernardini *et al.* 2013).

The DNS have been carried out in a $(L_x \times L_y \times L_z) = (6\pi h \times 2h \times 2\pi h)$ computational box, which is expected to be sufficiently long to accommodate the largest outer-layer flow structures based on previous DNS results at lower Reynolds number (Flores & Jimenez 2010). The mesh spacing in the wall-parallel directions has been kept (nearly) the same in wall units for all simulations. A cosine stretching function ($y(\xi) = -\cos(\pi(\xi + 1)/2)$, $\xi = [-1; 1]$) has been used to cluster points in the wall-normal direction, in such a way that the first point off the wall lies at $\Delta y_w^+ \approx 0.01$, and the maximum spacing in terms of local Kolmogorov units is $(\Delta y/\eta)_{max} \approx 1.84$, for all flow cases, where $\eta = (\nu^3/\varepsilon)^{1/4}$, $\varepsilon = 2\nu \overline{s'_{ij}s'_{ij}}$. Furthermore, since $\eta_w^+ \approx 1.5$, the resolution in the wall-parallel directions is $\Delta x/\eta \lesssim 6.5$, $\Delta z/\eta \lesssim 4.5$ throughout. Details on the computational mesh and on the flow parameters for the DNS are provided in table 1.

The simulations have been initiated with a laminar parabolic Poiseuille velocity profile, with maximum velocity u_p at the centerline, and bulk velocity $u_b = 2/3\, u_p$. After an initial transient, the pressure gradient starts to fluctuate about a nearly constant value, at the end of which spatial averages of the instantaneous fields in wall-parallel planes are taken at time intervals of $\Delta t = h/u_p$. The time window used for averaging, reported in table 1 in terms of the turnover periods for eddies of size h and typical velocity u_τ, is comparable to that used in previous studies (Hoyas & Jiménez 2006). The time history of the streamwise velocity variance at $y^+ = 15$ (averaged in the wall-parallel plane) is shown in figure 1. Note that, for the sake of comparison among the flow cases, the same time window is used, with an arbitrary time origin. The figure shows that the space averages oscillate in time with excursions of a few percent, at most, without significant drift, which suggests that time stationarity is achieved in all computations.

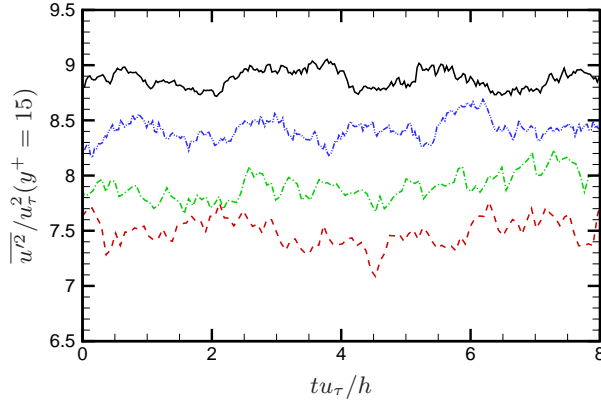The adequacy of the mesh used for the DNS has been verified through a grid sen-

Figure 1: Time evolution of streamwise velocity fluctuations at $y^+ = 15$ averaged in the wall-parallel plane, in inner units. The time origin is arbitrary. See table 1 for line legend.
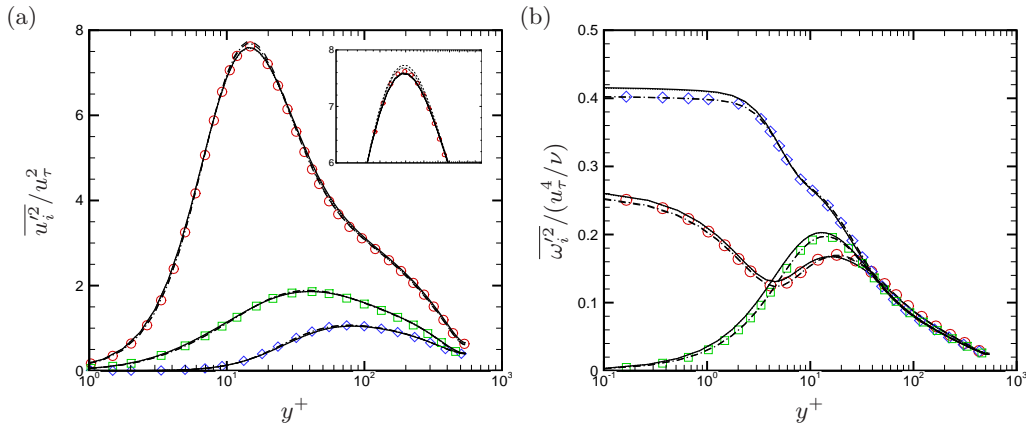

Figure 2: Grid sensitivity study for the CH1 flow case: distribution of (a) velocity variances ($i = 1$, circles; $i = 2$, diamonds; $i = 3$, squares) and (b) vorticity variances ($i = 1$, circles; $i = 2$, diamonds; $i = 3$, squares). Solid lines: baseline resolution ($\Delta x^+ = 10.1, \Delta z^+ = 6.7$); dashed lines: doubled resolution ($\Delta x^+ = 5.1, \Delta z^+ = 3.4$); dash-dotted line: quadruple resolution ($\Delta x^+ = 2.5, \Delta z^+ = 1.7$); dots: long domain ($L_x = 12\pi h$). Symbols indicate data from pseudo-spectral DNS at $Re_\tau = 550$ (del Álamo & Jiménez 2003).

sitivity study carried out at the lowest Reynolds number (CH1 flow case), for reasons of computational feasibility. First, the influence of mesh resolution was established by successively halving the spacing in both wall-parallel directions. The results of the study are shown in figure 2 for the velocity variances (a) and the vorticity variances (b), and compared with reference DNS data (Hoyas & Jiménez 2006), which were obtained with a pseudo-spectral code. Convergence of the flow statistics is observed on the two finer meshes, whose results are very close to the pseudo-spectral data. For the baseline mesh, the observed scatter is small for the velocity fluctuations (less than 1% in the peak variance), and somewhat larger for the vorticity variances (O(3%) at most), consistent with the notion that the smallest flow scales are most affected by mesh resolution effects, and possibly by the accuracy of the flow solver (Bernardini *et al.* 2013). The mean velocity
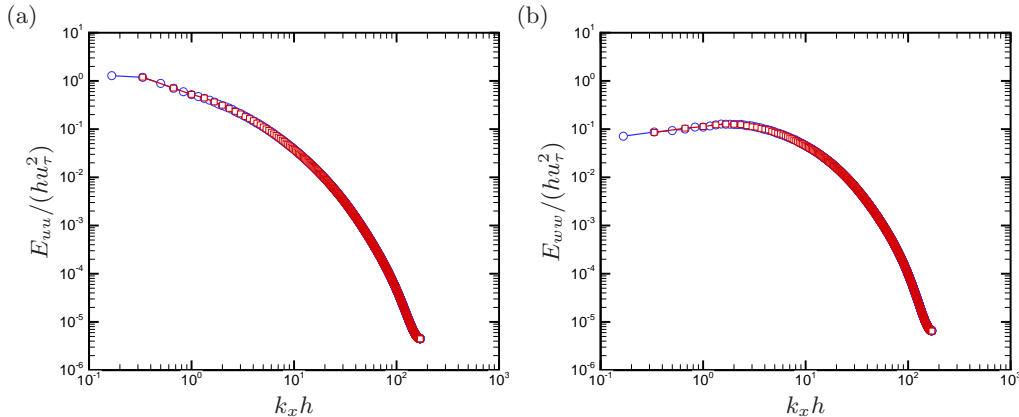
(a)

(b)

Figure 3: Effect of computational domain length on streamwise spectral densities at $y/h = 0.3$ for flow case CH1. Square symbols: $L_x = 6\pi h$; circles : $L_x = 12\pi h$. (a) spectra of u; (b) spectra of w.

profiles (not shown) exhibit scatter among the various curves by no more than 0.1%. Overall, we believe that these findings qualify second-order finite differences for DNS of wall-bounded turbulence.

The effect of the computational box size has also been addressed, by performing a DNS with the same spatial resolution as the CH1 flow case, on a computational box with doubled length ($L_x = 12\pi h$). The velocity and vorticity statistics, shown in figure 2 with dots, do not highlight any visible difference with the baseline CH1 data (indeed, the curves are indistinguishable in the selected representation). A comparison of the velocity spectra taken in the outer layer at $y/h = 0.3$ is provided in figure 3. Even though some energy is present at the longest resolved scales of motion, this is still well represented on the baseline mesh, as indicated by the near coincidence of the spectra on the two domains. The results of the grid-sensitivity study here carried out for $Re_\tau = 550$ can be extrapolated to higher Reynolds numbers with some caution, on the grounds that: i) the near-wall turbulence scales in wall units, hence keeping the same grid resolution in wall units is likely to preserve the quality of the results in this region; ii) the size of the outer-layer eddies scales on h, hence the size of the computational box is kept the same for all DNS. Although the two assumptions may be criticised, we believe that they are reasonably accurate for the present study, in which the Reynolds number varies over less than a decade. As a final check, the mean velocity profiles and the velocity variances are compared in figure 4 to the reference DNS data of Hoyas & Jiménez (2006) at $Re_\tau = 2003$, which shows a similar level of error as at lower Reynolds number, granted the validity of the pseudo-spectral data.

3. Results

3.1. *Velocity statistics*

The mean streamwise velocity profiles for the CH1-4 simulations are shown in Fig. 5(a), together with recent experimental data (Schultz & Flack 2013), at Reynolds numbers very close to those of the CH2-4 simulations. Figure 5 highlights the onset of a layer with nearly logarithmic velocity variation, whose extent visually increases with Re_τ, and excellent agreement with experiments. Fitting the CH4 data with a logarithmic velocity distribution $\overline{u}^+ = 1/k \log y^+ + C$ yields $k \approx 0.386$, $C \approx 4.30$, which are not too far, but
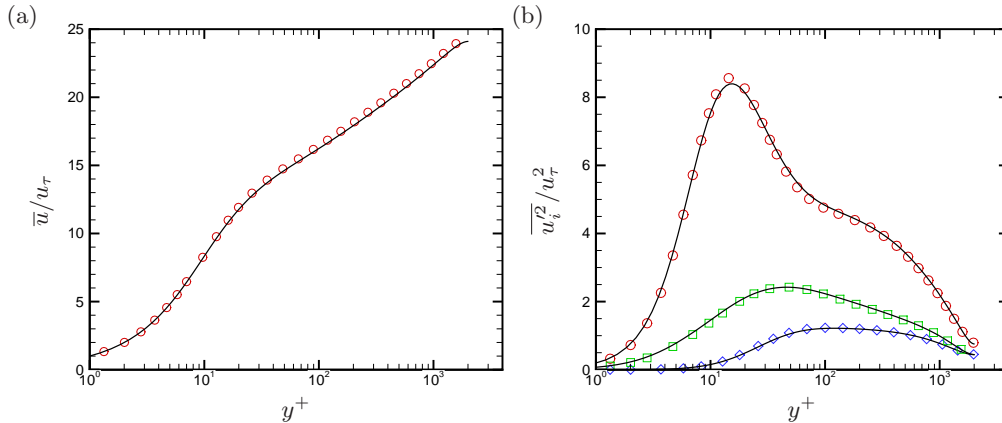
(a)

(b)

Figure 4: Comparison with pseudo-spectral DNS at $Re_\tau = 2000$: distribution of (a) mean velocity and (b) velocity variances. Solid lines: CH3 data; symbols: data from Hoyas & Jiménez (2006).

still sensibly different than the set of constants $k = 0.37$, $C = 3.7$, quoted by Nagib & Chauhan (2008) to be appropriate for channel flow.

   More refined information on the behavior of the mean velocity profile can be gained from inspection of the log-law diagnostic function

$$\Xi = y^+ \, \mathrm{d}\overline{u}^+/\mathrm{d}y^+, \tag{3.1}$$

shown in figure 5(b), whose constancy would imply the presence of a logarithmic layer in the mean velocity profile. For reference, in figure 5(b) we also show the trends of the defect-layer velocity profile derived by Townsend (1976, p. 147), under the assumption of uniform eddy viscosity

$$u_{CL}^+ - \overline{u}^+ = \frac{1}{2} R_s (1 - y/h)^2, \tag{3.2}$$

which implies

$$\Xi = R_s y/h (1 - y/h), \tag{3.3}$$

where u_{CL} is the mean velocity at the channel centerline, and R_s is a constant to be determined empirically. Specifically, the curves drawn in figure 5(b) were obtained using $R_s = 14$.

   The figure supports universality of the mean velocity in inner units up to $y^+ \approx 100$, where the diagnostic function attains a minimum, and the presence of a maximum whose position scales in outer units, at $y/h \approx 0.5$. Between those two extreme regions the distribution varies with the Reynolds number. While for $Re_\tau \lesssim 1000$ the diagnostic function connects the inner-layer minimum with the outer-layer maximum monotonically, an inflection point forms for $Re_\tau \gtrsim 2000$, which yields a region of linear variation extending from $y^+ \approx 600$ to $y/h \approx 0.5$, based on the present data. Approximate linear variation of the diagnostic function was also observed by Jiménez & Moser (2007), who, also based on the refined overlap arguments of Afzal & Yajnik (1973), proposed the following fit

$$\Xi = \frac{1}{k} + \alpha \frac{y}{h} + \frac{\beta}{Re_\tau}, \tag{3.4}$$

where α, β are adjustable constants, and k is the equivalent of the von Kármán constant. Based on the CH3 and CH4 DNS data (fitted in the range of linear variation of Ξ)
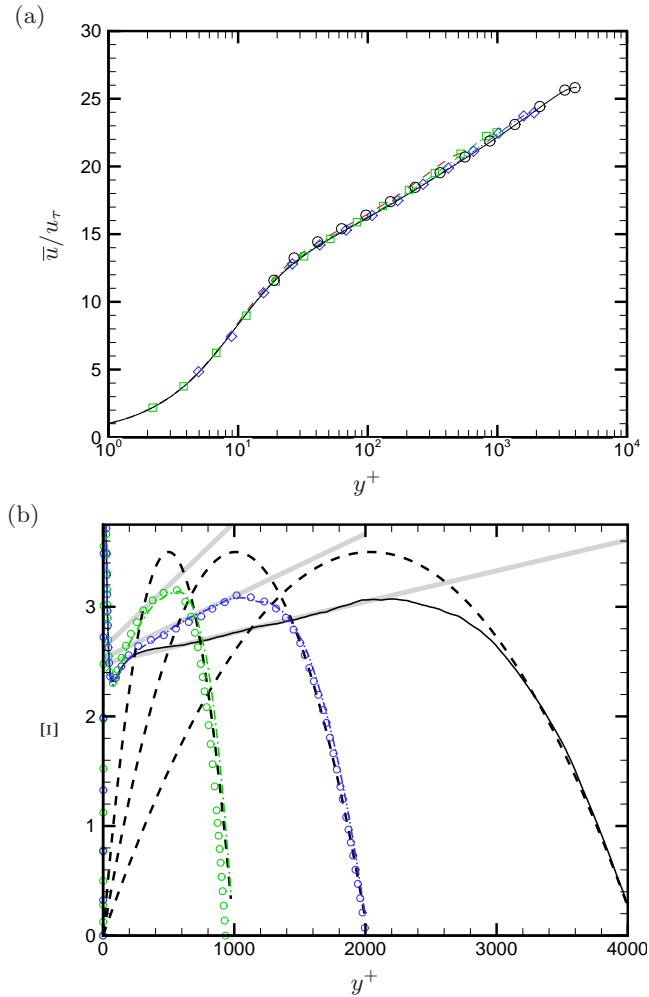
Figure 5: Distribution of mean velocity (a) and log-law diagnostic function (b), as defined in equation (3.1). In panel (a) the symbols indicate experimental data from Schultz & Flack (2013), at $Re_\tau = 1010$ (squares), $Re_\tau = 1956$ (diamonds), $Re_\tau = 4048$ (circles). In panel (b) the thick grey lines correspond to the generalized logarithmic profiles defined in equation (3.4), for Re_τ corresponding to the CH2-4 DNS; the thick dashed lines correspond to the defect-layer profiles defined in equation (3.3), and the symbols correspond to the DNS data of Hoyas & Jiménez (2006). See table 1 for nomenclature of the DNS data.

we obtain $k = 0.41$, $\alpha = 1.15$, $\beta = 180$, which are not too different from the set of constants suggested by Jiménez & Moser (2007) ($k = 0.40$, $\alpha = 1$, $\beta = 150$). The resulting plots are shown as solid grey lines in figure 5(b), which highlights the accuracy of the fit. The natural consequence of this behavior is that a genuine logarithmic layer is never achieved at any finite Reynolds number. Of course, at this stage we can only rely on the results of two DNS exhibiting inversion of the slope of the diagnostic function, which is the symptom of the onset of such generalized logarithmic layer. In this respect, available experiments are not very useful as they typically yield significant scatter in
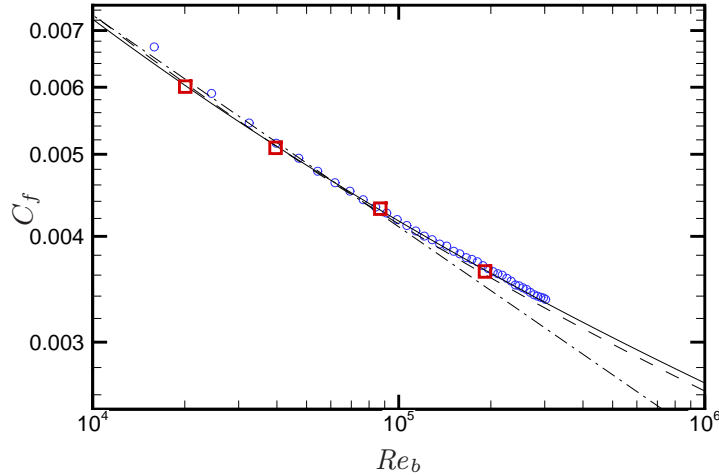
Figure 6: Comparison of skin friction coefficient with correlations and experiments. Square symbols denote DNS from CH1-4 datasets, and circles experimental data (Schultz & Flack 2013). The solid line indicates the friction law (3.5) with $k = 0.386$, $C = 4.30$; the dashed line indicates the friction law (3.5) with $k = 0.37$, $C = 3.7$; the dot-dashed line indicates Dean's friction law (equation (3.6)).

the diagnostic function graph. Hence, DNS at higher Reynolds number would be most welcome to confirm or refute our findings, and possibly determine more accurate values of the log-law constants in (3.4).

To verify possible alternatives to the logarithmic law (and its generalizations), we have also considered the diagnostic function for power-law behavior, namely $y^+/\overline{u}^+(\mathrm{d}\overline{u}^+/\mathrm{d}y^+)$, whose constancy would imply power-law variation of the mean velocity. The resulting distributions, not shown, have no significant plateau, which leads us to believe that the logarithmic law is more robust than the power law, in agreement with most current literature on the subject (Marusic *et al.* 2010).

Strictly related to the behavior of the mean velocity profile is the friction law. Early studies proposed approximations based on either log-law representations of the whole mean velocity profile, such as the classical Prandtl's smooth flow formula (Durand 1935)

$$\sqrt{\frac{2}{C_f}} = \frac{1}{k}\log\left(\frac{Re_b}{2}\sqrt{\frac{C_f}{2}}\right) + C - \frac{1}{k}, \qquad (3.5)$$

and power-law representations, such as Dean's (Dean 1978)

$$C_f = 0.073 Re_b^{-0.25}, \qquad (3.6)$$

where $C_f = 2\tau_w/(\rho u_b^2)$, $Re_b = 2hu_b/\nu$, and $u_b = \int_0^{2h}\overline{u}\,\mathrm{d}y/(2h)$ is the bulk velocity. In figure 6 we show the DNS data together with experimental data from Schultz & Flack (2013), compared with the semi-empirical curve-fits. The DNS data are in overall good agreement with experiments, albeit with systematic deviations of about 1%, which are however within the range of experimental uncertainty (Schultz & Flack 2013). It is also clear that Dean's power-law fit rapidly loses accuracy at high Reynolds number, and once a sensible log layer is formed, Prandtl's formula is clearly superior. We have tested Prandtl's formula (as given in equation (3.5), with two different sets of log-law coefficients, those suggested by Nagib & Chauhan (2008), and those derived from fitting the present DNS data. While the discrepancies are minor at low Reynolds number ($Re_b \lesssim 2\cdot 10^5$),
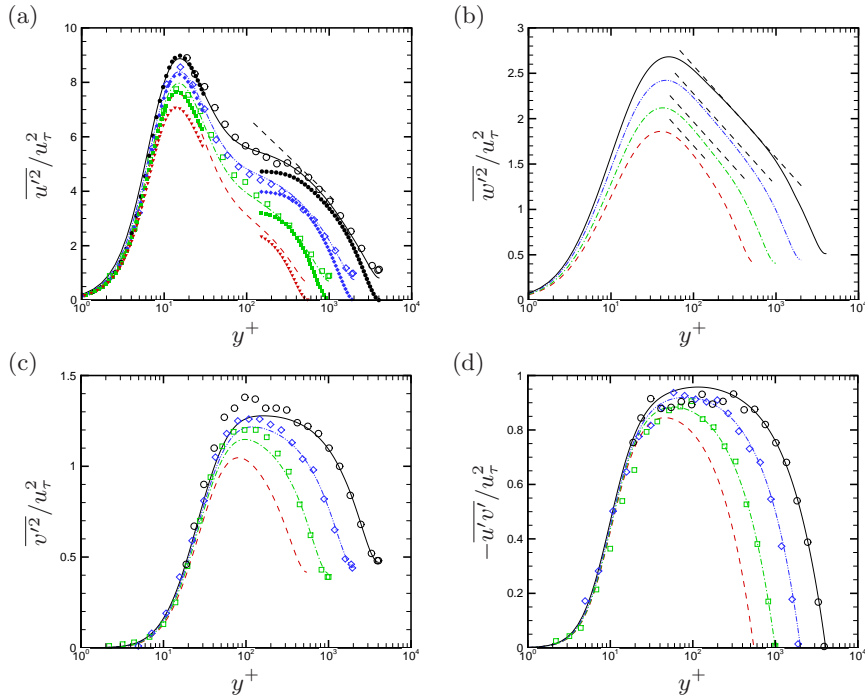
Figure 7: Distribution of Reynolds stress components across the channel. Symbols open symbols indicate experimental data from Schultz & Flack (2013), at $Re_\tau = 1010$ (squares), $Re_\tau = 1956$ (diamonds), $Re_\tau = 4048$ (circles). The solid symbols indicate curve fits obtained with the formulation of Marusic & Kunkel (2010). The dashed diagonal line in (a) denotes the distribution given in equation (3.7) for $B_1 = 2.1$ $A_1 = 1.26$, $Re_\tau = 4000$, and the dashed diagonal lines in (b) denote the distribution given in equation (3.8), with $A_3 = 0.44$, $B_3 = 0.95$. Refer to table 1 for nomenclature of the DNS data.

where Nagib's set of coefficients seems to be in closer agreement with the available data, the reverse behavior is found at higher Re_b, although no clear preference can be given to any set of constants.

The second-order velocity fluctuations statistics are shown in inner coordinates in figure 7, and their peaks are shown in figure 8 as a function of Re_τ. The main impression gained from the figure is that the trends observed at lower Reynolds number (Hoyas & Jiménez 2006) continue to hold. Specifically, the longitudinal stress (a) shows evident lack of universality in inner scaling, with fluctuation amplitudes which increase nearly logarithmically with Re_τ.

This behavior has been attributed (Metzger & Klewicki 2001; del Álamo *et al.* 2004; Mathis *et al.* 2009) to the increasing influence of inactive outer-layer modes on the near-wall dynamics. At this Reynolds number, no clear range with logarithmic variation of the streamwise velocity variance is observed, as predicted by the attached eddy hypothesis (Townsend 1961; Perry & Li 1990), and for which experiments in boundary layers and pipes at much higher Reynolds number suggest (Marusic *et al.* 2013)

$$\overline{u'^2}/u_\tau^2 \approx B_1 - A_1 \log(y/h), \tag{3.7}$$

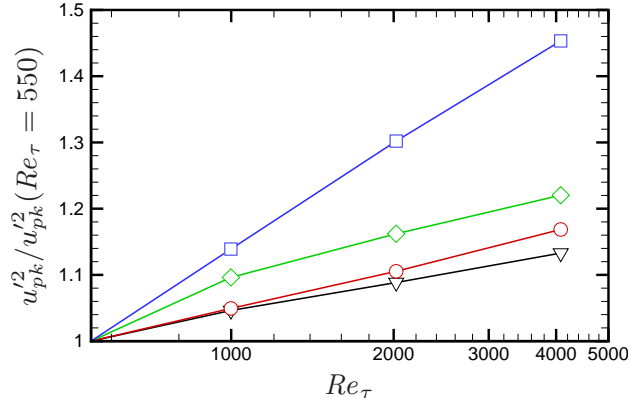with $A_1 \approx 1.26$, which we have tentatively sketched in the figure. The spanwise velocity

Figure 8: Peak velocity variances as a function of Re_τ, normalized by their value at $Re_\tau = 550$. Symbols: u, circles; v, diamonds; w, squares; uv, gradients.

fluctuations (b) have a similar behavior, with substantial dependence of the inner-scaled intensities on Re_τ. In this case, the formation of an extended logarithmic layer is much more evident, and we find evidence for a universal scaling

$$\overline{w'^2}/u_\tau^2 \approx B_3 - A_3 \log(y/h), \tag{3.8}$$

with $A_3 \approx 0.44$, $B_3 \approx 0.95$, first found by Jiménez & Hoyas (2008) at lower Re_τ (with $A_3 \approx 0.5$, $B_3 \approx 0.8$). The wall-normal velocity fluctuations (c) exhibit universality in inner scaling in a wider part of the near-wall region, but their peak still grows with Re_τ, even though the growth is sub-logarithmic, and probably $\overline{v'^2}$ tends to saturate as $\overline{u'v'}^+$ approaches the unit value (d). Furthermore, no evident plateau of $\overline{v'^2}$ (predicted by the attached-eddy hypothesis) has formed at the Reynolds numbers of this study. Overall, it should be noted that the agreement of the observed trends with experiments is excellent, except perhaps for the peak of the wall-normal velocity, which is by the way notoriously difficult to measure. The agreement with the similarity formulation for the streamwise turbulence intensity proposed by Marusic & Kunkel (2010), and based on an extension of the attached eddy hypothesis, is also satisfactory.

Velocity variances are shown in (u_τ, h) scaling in figure 9, to highlight outer-layer trends. Clear collapse of the distributions is observed for the spanwise velocity fluctuations, whereas violation of the u_τ scaling is observed for the streamwise velocity fluctuations. This discrepancy was first noticed by DeGraaff & Eaton (2000), who attributed it to the effect of large-scale motions scaling with the velocity at the edge of the wall layer (in this case, the mean centerline velocity). Later (del Álamo *et al.* 2004), it became clear that the increase of u' at fixed y/h is associated with h-scaled outer-layer modes which are superposed onto the wall-attached modes, which scale on u_τ. Here (figure 9b), consistent with the findings of DeGraaff & Eaton (2000), it is found that scaling u' by $u_{MIX} = (u_\tau u_{CL})^{1/2}$ effectively removes this dependency, and collapse of the streamwise velocity is observed for $y/h \gtrsim 0.2$. Further explanation for the observed scaling is provided later on. More ambiguous is the behavior of v'. Inspection of figure 9(c-d) shows than none of the two velocity scalings is able to remove the Re_τ dependency. However, as also found for the inner layer, the u_τ scaling seems to yield a flat asymptotic behavior at the highest Re_τ available, which leads us to suspect that lack of universality is a low-Reynolds-number effect.

A visual impression of the effect of outer-scaled eddies on the near-wall layer can be gained from Fig. 10, where we show velocity fluctuation contours in wall-parallel
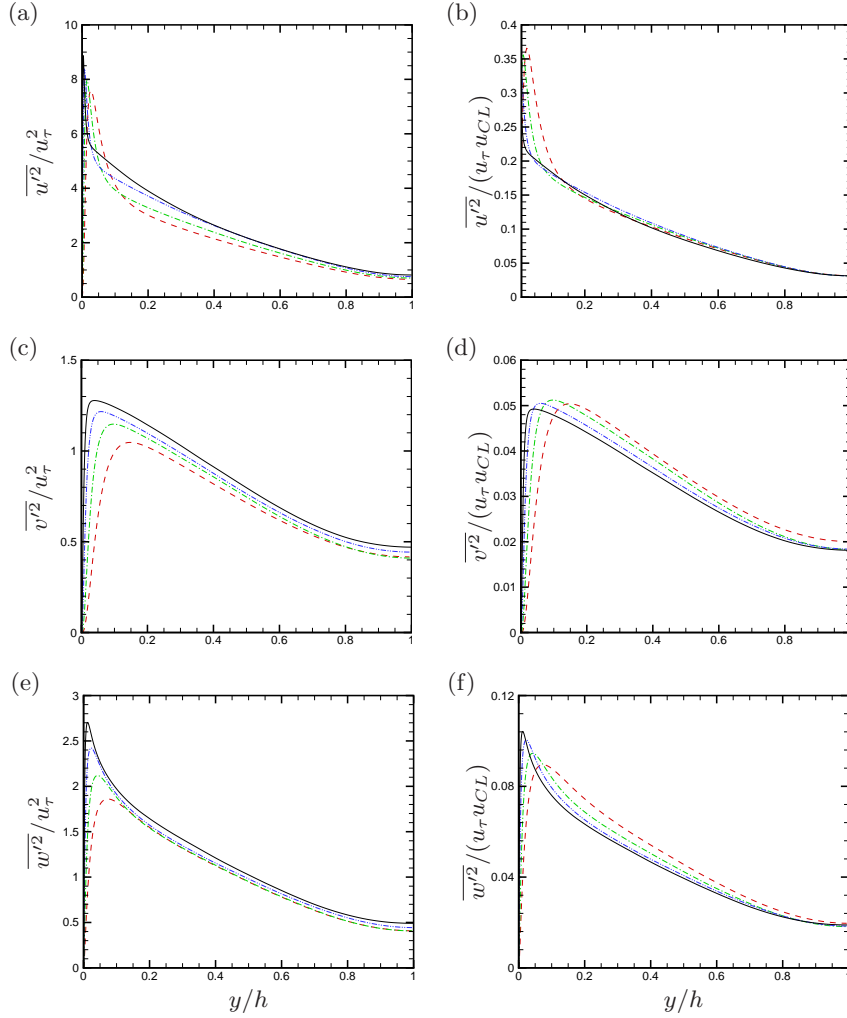
Figure 9: Distribution of Reynolds stress components in outer scaling (a,c,e) and mixed scaling (b,d,f). See table 1 for nomenclature of the DNS data.

planes at $y^+ \approx 15$, which corresponds to the position of the peak of streamwise velocity fluctuations, and in the outer layer, at $y/h = 0.3$. A two-scale organization is clearly visible at $y^+ = 15$, with high- and low-momentum streaks having width of the order of 100 wall units, which are part of the inner-layer turbulence sustainment cycle (Smith & Metzler 1983; Jiménez & Pinelli 1999), and superposed on them much larger streaks, having size of the order of h. While this effect was previously noticed in DNS at lower Reynolds number (Hutchins & Marusic 2007), the scale separation and imprinting effects here are much more prominent. The flow organization in cross-stream planes is monitored in figure 11, where we show the contours of velocity fluctuations. It appears that the core flow is mainly organized into 'towering' eddies which are attached to the wall, and which occupy the entire half-channel in which they are generated. Significant correlation of u' and v' events is observed (negative in the lower half of the channel, positive in the upper half), which points to a non-negligible contribution of these eddies to the Reynolds stress far from the walls. Less clear is the organization of w'. In the classical
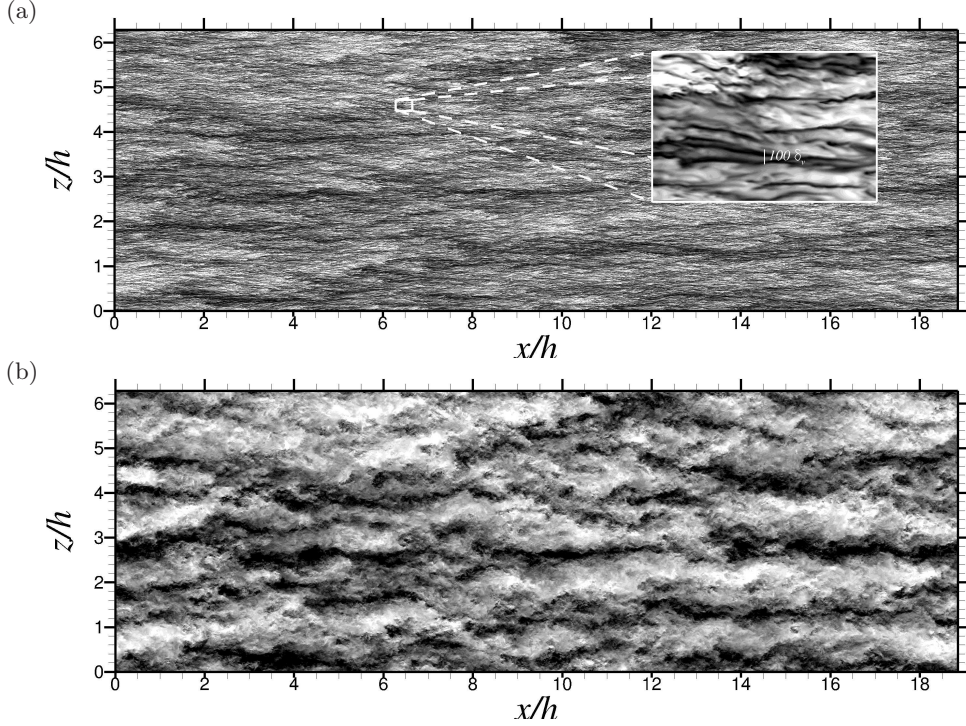
(a)

(b)

Figure 10: Instantaneous streamwise velocity field in $x-z$ planes at $y^+ = 15$ (a), $y/h = 0.3$, for the CH4 dataset. Contour levels are shown for $-1.77 \leqslant u'/u_{\mathrm{rms}} \leqslant 1.77$ (a), and $-1.96 \leqslant u'/u_{\mathrm{rms}} \leqslant 1.96$ (b), from dark to light shades. The figure inset in (a) shows a zoom of a $(1500^+ \times 1000^+)$ box, to highlight viscous length scales.

picture (del Álamo & Jiménez 2006), outer-layer streaks (i.e. u' events) are associated with rollers, hence spanwise velocity fluctuations should have a quadrupolar distribution around positive/negative u' events. However, this pattern is not easy to discern in the flow visualizations.

3.2. *Velocity spectra*

Spectral densities of the velocity fluctuations are shown in figure 12 for the inner layer, and in figure 13 for the outer layer. Note that wavelengths ($\lambda_i = 2\pi/k_i$) are shown on the horizontal axis, rather than the corresponding wavenumbers, to more clearly highlight the eddies length scales. Further, the spectra are pre-multiplied by the wavenumber, in order that equal areas correspond to equal energies in a logarithmic plot. Consistent with expectations, inner scaling yields collapse of the spectra at the smallest resolved scales of motion across the range of Reynolds numbers, whereas outer scaling yields (approximate) collapse of the large scales. The inner-layer spectra clearly show the presence of an energetic inner site corresponding to the near-wall streak regeneration cycle. The typical length scales in the spanwise direction remain very roughly universal, with $\lambda_z^u \approx \lambda_z^w \approx 100\delta_v$, $\lambda_z^v \approx 50\delta_v$, which in the classical interpretation (Hamilton *et al.* 1995), correspond to the near-wall streaks/streamwise vortices system. Additional energy appears at large wavelengths in the u and w spectra as Re_τ increases, as a result of outer-layer imprinting processes. A k_z^{-1} range in the streamwise velocity spectra, whose presence is predicted by the attached eddy hypothesis (Perry & Abell 1977; Nickels *et al.*
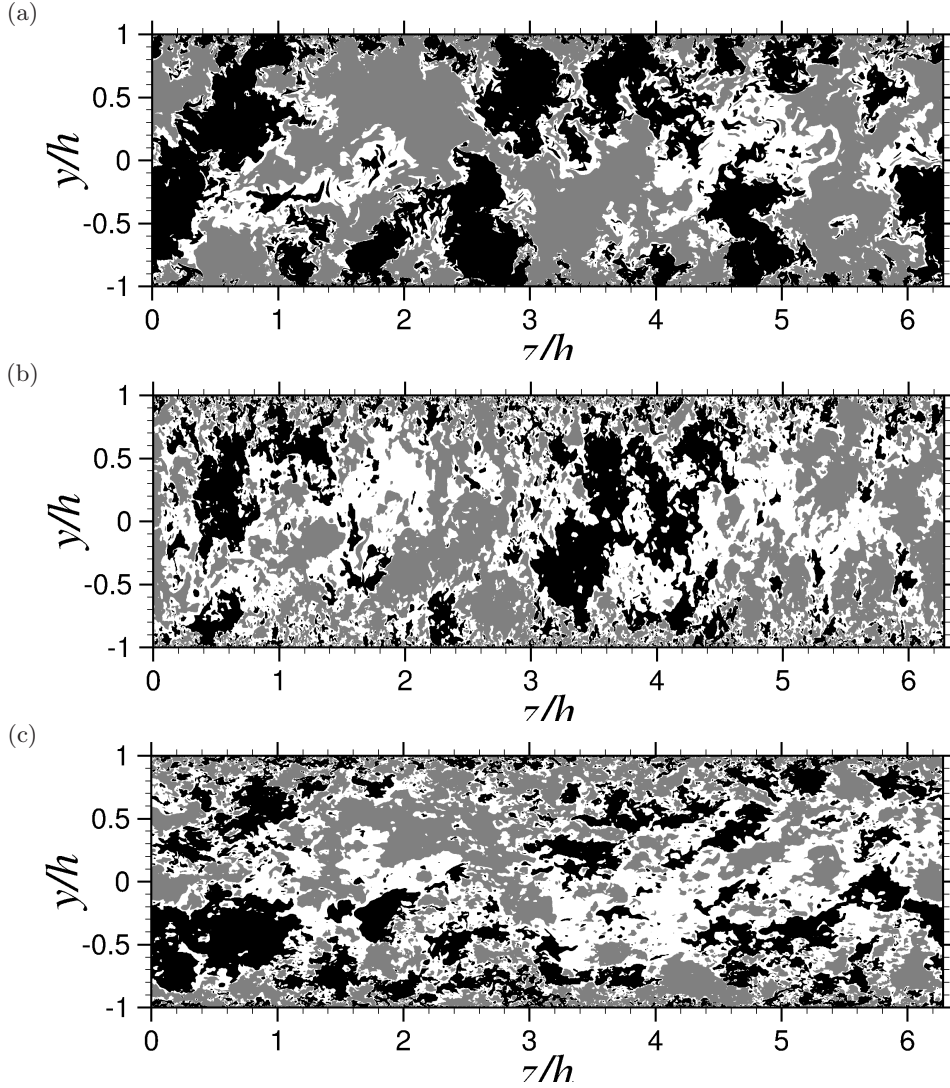
(a)

(b)

(c)

Figure 11: Instantaneous cross-stream visualizations of u' (a), v' (b), w' (c) for the CH4 dataset. Contour levels below $-0.5u_\tau$ are shown in black, and contour levels above $0.5u_\tau$ are shown in grey.

2005) at sufficiently high Re_τ, is not clear based on the present data, even though its emergence might be suggested by the small plateau in the pre-multiplied spectra at $Re_\tau = 4000$. The spanwise spectral densities (figure 13) exhibit a qualitatively similar organization as the inner-layer spectra, but on a different scale. Specifically, the typical length scales of the eddies are $\lambda_z^u \approx \lambda_z^w \approx h$, $\lambda_z^v \approx h/2$, which suggests that the large-scale organization of the flow still consists of streaks coupled with rollers. It is noteworthy that, while the spanwise spectra of v and w are relatively broad-banded, and tend to be weakly affected by Re_τ, those of u tend to exhibit a sharp peak as Re_τ increases. This feature is difficult to observe in experiments, which typically can only access streamwise spectra upon use of Taylor's hypothesis, and it is likely caused by the activation of the outer-layer modes through a transient growth mechanism (Hutchins & Marusic 2007; del
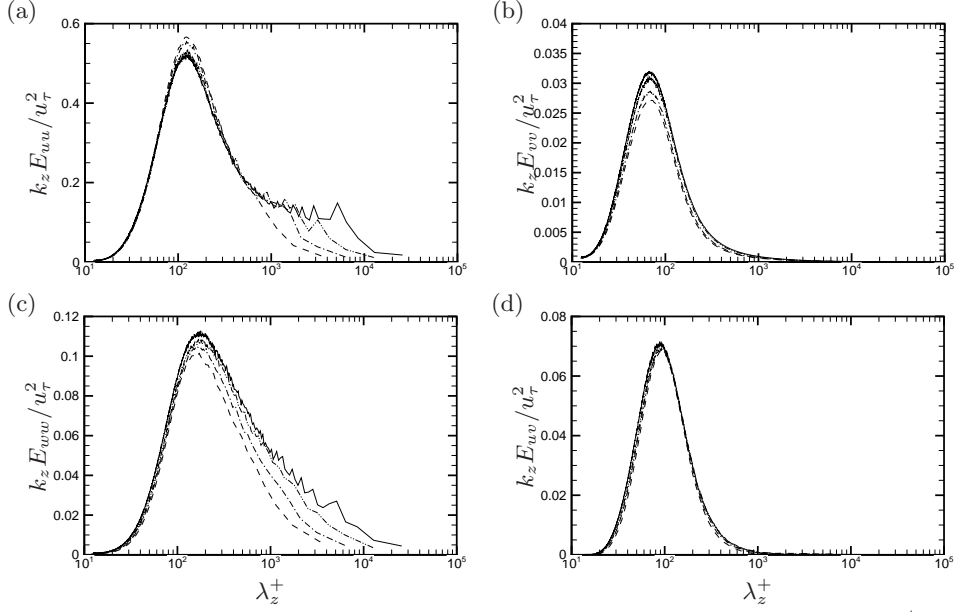
Figure 12: Pre-multiplied spanwise spectral densities of velocity fluctuations at $y^+ = 15$. (a) u-spectra; (b) v-spectra; (c) w-spectra (d) uv co-spectra.
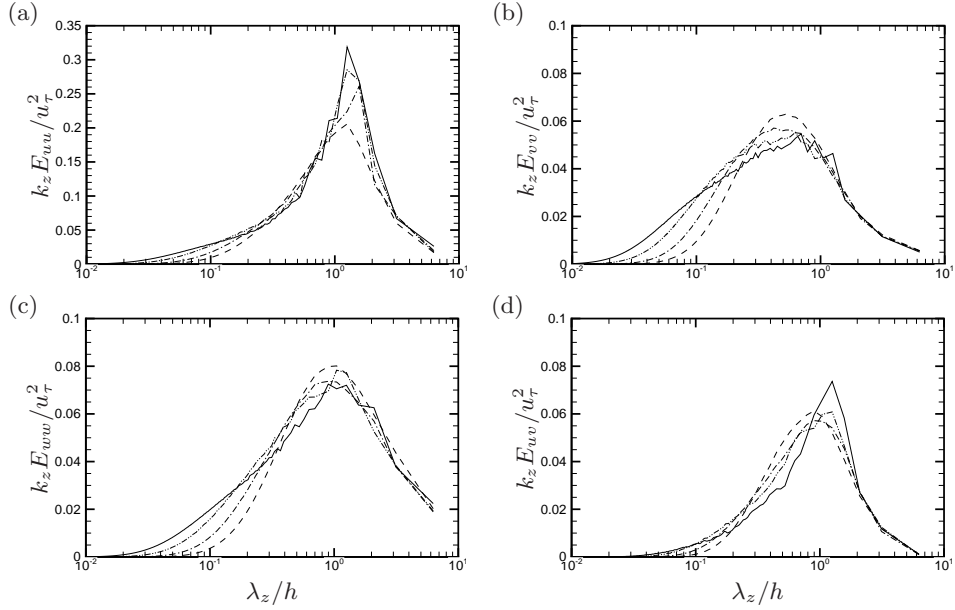

Figure 13: Pre-multiplied spanwise spectral densities of velocity fluctuations at $y/h = 0.3$. (a) u-spectra; (b) v-spectra; (c) w-spectra (d) uv co-spectra.

Álamo & Jiménez 2006). This observation is further corroborated from the uv co-spectra, shown in figure 13(d), which can be interpreted as spectra of turbulence kinetic energy production (at a given off-wall distance), and which exhibit the same spikes as the u spectra.

Clearer control on the structural flow changes with Re_τ is obtained from figure 14,
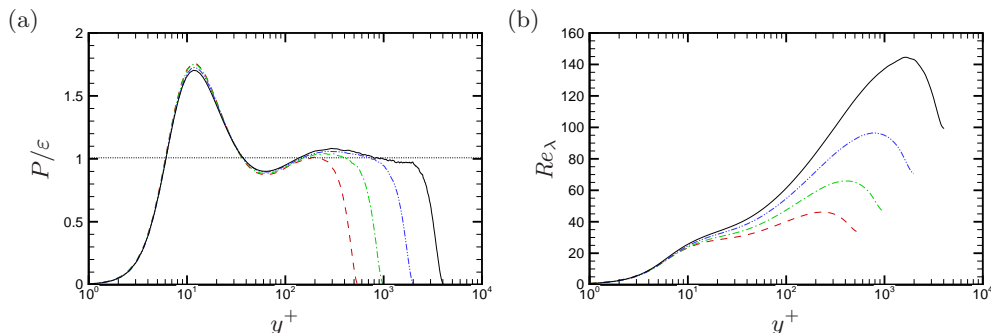
Figure 14: Distribution of the production/dissipation ratio (a), and of the Taylor-scale Reynolds number (b).

where we show the distribution of the production-to-dissipation ratio, P/ε (where $P = -(\mathrm{d}\overline{u}/\mathrm{d}y)\overline{u'v'}$), and of the effective Taylor-scale Reynolds number, defined as $Re_\lambda = \lambda q/\omega_{rms}$, with $\lambda = q/\omega_{rms}$ (where $q^2 = \overline{u_i'u_i'}$ is the velocity fluctuation variance, and ω_{rms} is the root-mean-square vorticity). The most noticeable feature of figure 14a is the slow (but steady) increase of P/ε with Re_τ in the outer layer, where it attains a plateau. In fact, production exceeds dissipation for $Re_\tau \gtrsim 1000$, by up to 8% in the CH4 simulation, over a significant fraction of the outer wall layer. This effect was first speculated by Bradshaw (1967), and it was not noticed in early DNS at limited Reynolds number (Mansour *et al.* 1988). A little production excess was observed to emerge in channel flows only at $Re_\tau \gtrsim 1000$ (Hoyas & Jiménez 2008). From a physical standpoint, this finding implies that the excess turbulence kinetic energy shall be transferred to the underlying layers through turbulent diffusion (convection and pressure). Indeed, the only other term left in the kinetic energy budget is viscous diffusion, which is negligible throughout the outer layer. This observation points to the activation of top-down mechanisms of influence, in addition to the conventional bottom-up scenario (Hunt & Morrison 2001). The Taylor Reynolds number (figure 14b) is observed to increase in the outer layer, attaining values which make it possible the formation of inertial ranges in the velocity spectra. The presence of power-law ranges in the velocity spectra is verified in figure 15, where data are shown in Kolmogorov units, at $y/h = 0.3$, which roughly coincides with the peak location of Re_λ. The spectra are reported in compensated form, in such a way that a plateau corresponds to a power-law range, and compared with forced isotropic turbulence data at $Re_\lambda = 142$ (Jiménez *et al.* 1993), to verify the accuracy in the prediction of the small scales of turbulence. The streamwise spectrum of u highlights the presence of a decade with $k^{-1.48}$ variation, which is significantly less steep than Kolmogorov's $k^{-5/3}$ inertial spectrum. Similar deviations from the ideal behavior were observed in experiments of grid turbulence (Mydlarski & Warhaft 1996), and homogeneously sheared flow (Ferchichi & Tavoularis 2000), and attributed to low-Reynolds number effects. In particular, Mydlarski & Warhaft (1996) proposed a fit for the scaling exponent of the longitudinal spectra,

$$E(k) \sim k^{5/3-p}, \quad p = 5.25 Re_\lambda^{-2/3}. \tag{3.9}$$

For $Re_\lambda \approx 140$ (which corresponds to the outer-layer value of the CH4 DNS), the resulting exponent is comparable with our observations. Similar conclusions also hold for the transverse spectra (v and w), which exhibit power-law behavior with yet smaller slope than the longitudinal ones. On the other hand, the spanwise spectra of u show the formation of a narrow $k^{-5/3}$ spectral band (limited to the CH4 case) between the large-scale
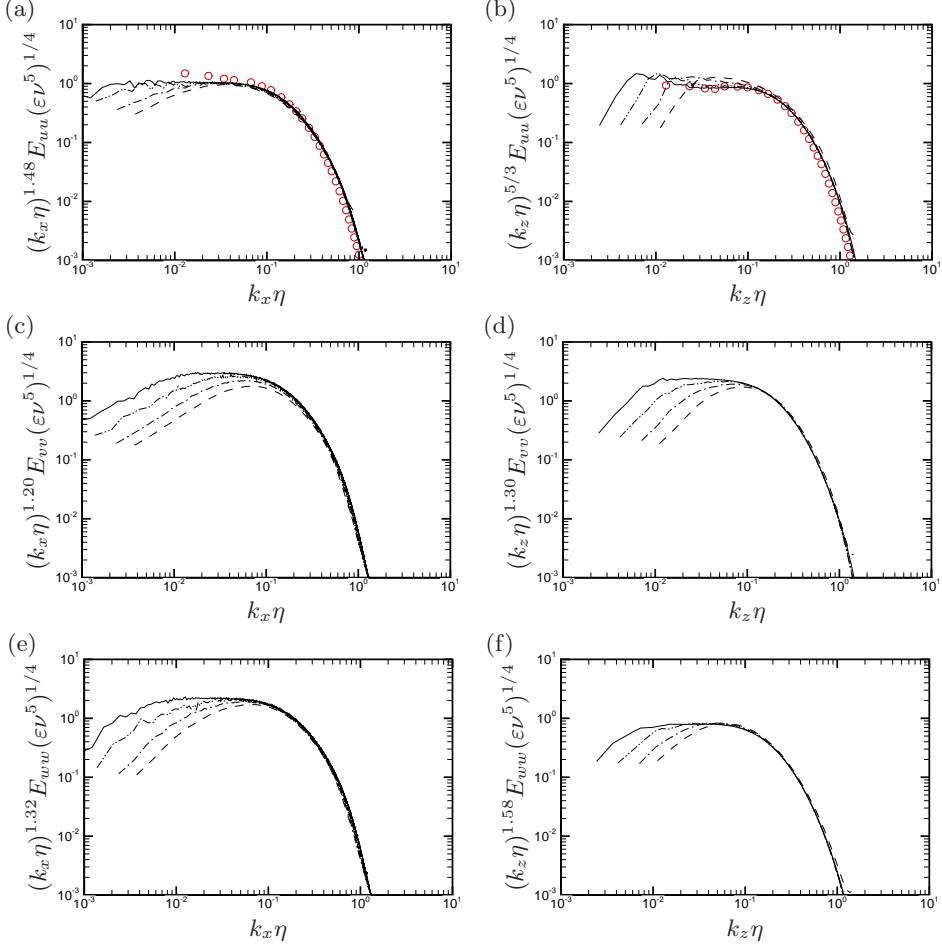
Figure 15: Compensated spectral densities of velocity fluctuations at $y/h = 0.3$ in the streamwise direction (left column) and in the spanwise direction (right column). The exponent used for compensation (p) was determined for each case as the value for which a wider plateau was observed in the CH4 flow case. The symbols indicate isotropic turbulence data at $Re_\lambda = 142$ (Jiménez *et al.* 1993). See table 1 for nomenclature of DNS data.

peak and the dissipative range, whereas power-law ranges with exponents different than $-5/3$ are observed for v and w. This behavior can be tentatively ascribed to the fact that energy is mainly pumped into the streamwise velocity mode through forcing acting at a discrete spanwise wavenumber, which translates into the sharp spectral peak of u at $\lambda_z \approx h$. Such forcing is not found either in the other two velocity components, nor in any streamwise spectra. Since Kolmogorov's theory is based on the assumption that energy if fed into the system only at the largest scales of motion, and on the assumption of scale separation with the dissipative scales, it is then natural that Kolmogorov spectra are more easily observed in the spanwise spectra of u, where production is concentrated. Again, we point out that this type of analysis is difficult in experiments, and as a matter of fact, clear Kolmogorov spectra were not observed in longitudinal spectra, even at much
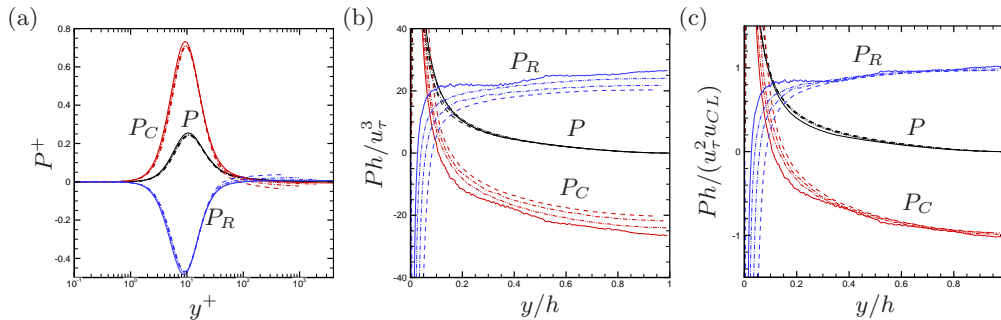
Figure 16: Contributions to turbulence kinetic energy production in inner units (a), and in outer coordinates, with standard outer normalization (b), and with 'mixed' normalization (c).

higher Reynolds number (Saddoughi & Veeravalli 1994; McKeon & Morrison 2007). In this sense, the use of DNS at high Reynolds number can provide a useful contribution.

3.3. *Analysis of turbulence kinetic energy production*

Further insight into the mechanisms of turbulence kinetic energy production can be gained by considering the following decomposition of the kinetic energy production term (Orlandi 1997)

$$P = -\overline{u'v'}\frac{\mathrm{d}\overline{u}}{\mathrm{d}y} = \underbrace{\overline{u}\left(\overline{w'\omega_y'} - \overline{v'\omega_z'}\right)}_{P_R} \underbrace{-\frac{\mathrm{d}}{\mathrm{d}y}\left(\overline{u}\,\overline{u'v'}\right)}_{P_C}, \tag{3.10}$$

whereby production it is split into a term (P_R) containing the streamwise component of the fluctuating Lamb vector ($\mathbf{p} = -\boldsymbol{\omega}' \times \mathbf{u}'$), where $\boldsymbol{\omega}' = \nabla \times \mathbf{u}'$, and which is an indicator of the rate of energy transfer to small scales (Rogers & Moin 1987), and a term in divergence form (P_C), which thus represents redistribution of kinetic energy production across the channel. The two terms in equation (3.10) are shown in figure 16 in inner and outer scaling. For that purpose, we note that the obvious inner normalization for P is by u_τ^3/δ_v. On the other hand, the natural outer normalization is by u_τ^3/h, assuming that u_τ is the only legitimate outer-layer velocity scale. The near-wall distributions, shown in figure 16(a), highlight close universality in wall units, and confirm the pattern found in pipe flow (Orlandi 1997), with accumulation of kinetic energy production associated with P_C, which is partly balanced by the energy flux from the large to the small scales. The opposite scenario holds away from the wall, where P_R is positive and P_C is negative, the crossover occurring near the peak position of the turbulent shear stress. In this case, the natural outer scaling is not capable of collapsing the distributions across the Re_τ range. We then consider an alternative scaling, which should hold for P_C, P_R and P. We focus on P_R, under the following assumptions: i) $v' \sim w' \sim u_\tau$, as confirmed from the analysis of the velocity variances; ii) $\omega_y' \sim \omega_z' \sim u_\tau/\delta_v$, which is the generally accepted scaling for the vorticity fluctuations, at least for $y^+ \gtrsim 10$ (e.g. Klewicki 2010); iii) $\overline{u} \sim u_{CL}$ in the outer layer. We then conclude

$$P \sim P_C \sim P_R \sim u_\tau^2 u_{CL}/h. \tag{3.11}$$

The scaling 3.11 is tested in figure 16(c), and shown to be much more accurate than the standard outer scaling for $y/h \gtrsim 0.2$. A consequence of this finding is that the streamwise velocity fluctuations should scale as $\overline{u'^2} \sim P/\tau$, where $\tau = h/u_\tau$ is the typical

eddy turnover time in the outer layer (Simens *et al.* 2009). Hence, it follows that

$$\overline{u'^2} \sim u_\tau u_{CL}, \qquad (3.12)$$

which coincides with the mixed scaling proposed by DeGraaff & Eaton (2000), as shown in figure 9b. The reader may consult Marusic & Kunkel (2010) for alternative explanation of the occurrence of mixed scaling.

4. Conclusions

Flow statistics from DNS at computationally high Reynolds number have been collected and commented. At the Reynolds number of the largest simulation ($Re_\tau \approx 4000$) some effects which are believed to be typical of the asymptotic high-Re regime start to manifest themselves.

A range with near logarithmic behavior of the mean velocity is observed in the mean velocity profiles. However, rather than being constant in the overlap layer, the log-law indicator function exhibits a linear increase whose slope decreases with the Reynolds number. A logarithmic layer would only be recovered in the infinite Reynolds number limit, for which the appropriate value of the von Kármán constant is $k \approx 0.41$. This behavior would be consistent with refined overlap arguments (Afzal & Yajnik 1973; Jiménez & Moser 2007), but data at yet higher Re_τ are certainly required to confirm its robustness.

Exploration of the high-Re regime also allows to verify other theoretical predictions, including the logarithmic decrement of the wall-parallel velocity variances with the wall distance (Townsend 1976). While clear and extended logarithmic ranges are observed for w', the same does not hold for u', which rather tends to form a plateau in the overlap layer, in the Reynolds number range under inquiry. This finding is perhaps due to the need for yet higher Reynolds numbers. It is also confirmed that, while v', w', and $u'v'$ scale with the friction velocity, as in the standard theory (except for low-Re effects), u' exhibits a mixed scaling, with $(u_\tau u_{CL})^{1/2}$ (DeGraaff & Eaton 2000). Justifications for the observed scaling are proposed, based on dimensional analysis applied to the kinetic energy production term. A limited spectral range with $k^{-5/3}$ Kolmogorov scaling is only observed for the outer-layer spanwise spectra of u', whereas all other longitudinal and transverse spectra exhibit power-law behavior with less steep slope. This behavior has been related to the presence of a sharply peaked spectral forcing, associated with $O(h)$ outer-layer modes, whose excess energy is transferred to the underlying layers through turbulent transport.

Flow statistics are available at the web page `http://grassopc.dma.uniroma1.it/channel/`, with supporting documentation.

REFERENCES

AFZAL, N. & YAJNIK, K. 1973 Analysis of turbulent pipe and channel flows at moderately large reynolds number. *J. Fluid Mech.* **61**, 23–31.

DEL ÁLAMO, J.C. & JIMÉNEZ, J. 2003 Spectra of the very large anisotropic scales in turbulent channels. *Phys. Fluids* **15**, L41–L44.

DEL ÁLAMO, J. C. & JIMÉNEZ, J. 2006 Linear energy amplification in turbulent channels. *J. Fluid Mech.* **559**, 205–213.

DEL ÁLAMO, J. C., JIMÉNEZ, J., ZANDONADE, P. & MOSER, R. D. 2004 Scaling of the energy spectra of turbulent channels. *J. Fluid Mech.* **500**, 135–144.

BERNARDINI, M. & PIROZZOLI, S. 2009 A general strategy for the optimization of rungekutta schemes for wave propagation phenomena. *J. Comp. Phys.* **228**, 4182 – 4199.

BERNARDINI, M, PIROZZOLI, S, QUADRIO, M & ORLANDI, P 2013 Turbulent channel flow simulations in convecting reference frames. *J. Comput. Phys.* **232**, 1–6.

BRADSHAW, P. 1967 Inactive motion and pressure fluctuations in turbulent boundary layers. *J. Fluid Mech* **30**, 241–258.

DEAN, R.B. 1978 Reynolds number dependence of skin friction and other bulk flow variables in two-dimensional rectangular duct flow. *Trans. ASME, J. Fluid Eng.* **100**, 215–223.

DEGRAAFF, D.B. & EATON, J.K. 2000 Reynolds-number scaling of the flat-plate turbulent boundary layer. *J. Fluid Mech.* **422**, 319–346.

DURAND, W.F. 1935 *Aerodynamic Theory*. Spinger.

FERCHICHI, M. & TAVOULARIS, S. 2000 Reynolds number effects on the fine structure of uniformly sheared turbulence. *Phys. Fluids* **12**, 2942–2953.

FLORES, O. & JIMENEZ, J. 2010 Hierarchy of minimal flow units in the logarithmic layer. *Phys. Fluids* **22**, 071704.

GUALA, M., HOMMEMA, S.E. & ADRIAN, R.J. 2006 Large-scale and very-large-scale motions in turbulent pipe flow. *J. Fluid Mech.* **554**, 521–542.

HAMILTON, J. M., KIM, J. & WALEFFE, F. 1995 Regeneration mechanisms of near-wall turbulent structures. *J. Fluid Mech.* **287**, 317348.

HOYAS, S. & JIMÉNEZ, J. 2006 Scaling of velocity fluctuations in turbulent channels up to $Re_\tau = 2003$. *Phys. Fluids* **18**, 011702.

HOYAS, S. & JIMÉNEZ, J. 2008 Reynolds number effects on the Reynolds-stress budgets in turbulent channels. *Phys. Fluids* **20**, 101511.

HULTMARK, M., BAILEY, S.C.C. & SMITS, A.J. 2010 Scaling of near-wall turbulence in pipe flow. *J. Fluid Mech.* **649**, 103–113.

HUNT, J.C.R. & MORRISON, J.F. 2001 Eddy structure in turbulent boundary layers. *Eur. J. Mech. B Fluids* **19**, 673–694.

HUTCHINS, N. & MARUSIC, I. 2007 Evidence of very long meandering features in the logarithmic region of turbulent boundary layers. *J. Fluid Mech.* **579**, 1–28.

JIMÉNEZ, J. & HOYAS, S. 2008 Turbulent fluctuations above the buffer layer of wall-bounded flows. *J. Fluid Mech.* **611**, 215–236.

JIMÉNEZ, J. & MOSER, R.D. 2007 What are we learning from simulating wall turbulence? *Phil. Trans. R. Soc. Lond. A* **365**, 715–732.

JIMÉNEZ, J. & PINELLI, A. 1999 The autonomous cycle of near–wall turbulence. *J. Fluid Mech.* **389**, 335–359.

JIMÉNEZ, J., WRAY, A. A., SAFFMAN, P. G. & ROGALLO, R. S. 1993 The structure of intense vorticity in isotropic turbulence. *J. Fluid Mech.* **255**, 65–90.

KIM, J. & MOIN, P. 1985 Application of a fractional-step method to incompressible Navier-Stokes equations. *J. Comput. Phys.* **59**, 308–323.

KIM, K.C. & ADRIAN, R.J. 1999 Very large-scale motion in the outer layer. *Phys. Fluids* **11**, 417–422.

KLEWICKI, J.C. 2010 Reynolds number dependence, scaling, and dynamics of turbulent boundary layers. *J. Fluids Eng.* **132**, 094001.

KLEWICKI, J. C. & FALCO, R. E. 1990 On accurately measuring statistics associated with small scale structure in a turbulent boundary layers using hot wire probes. *J. Fluid Mech.* **541**, 21–54.

MANSOUR, N.N., KIM, J. & MOIN, P. 1988 Reynolds-stress and dissipation-rate budgets in a turbulent channel flow. *J. Fluid Mech.* **194**, 15–44.

MARUSIC, I. & KUNKEL, G.J. 2010 Streamwise turbulence intensity formulation for flat-plate boundary layers. *Phys. Fluids* **22**, 051704.

MARUSIC, I., MCKEON, B.J., MONKEWITZ, P.A., NAGIB, H.M., SMITS, A.J. & SREENIVASAN, K.R. 2010 Wall-bounded turbulent flows at high Reynolds numbers: Recent advances and key issues. *Phys. Fluids* **22**, 065103.

MARUSIC, I., MONTY, J.P., HULTMARK, M. & SMITS, A.J. 2013 On the logarithmic region in wall turbulence. *J. Fluid Mech.* **716**.

Mathis, R., Hutchins, N. & Marusic, I. 2009 Large-scale amplitude modulation of the small-scale structures in turbulent boundary layers. *J. Fluid Mech.* **628**, 311–337.

McKeon, B.J. & Morrison, J.F. 2007 Asymptotic scaling in turbulent pipe flow. *Phil. Trans. R. Soc. Lond. A* **365**, 771–787.

Metzger, M.M. & Klewicki, J.C. 2001 A comparative study of near-wall turbulence in high and low Reynolds number boundary layers. *Phys. Fluids* **13**, 692–701.

Mydlarski, L. & Warhaft, Z. 1996 On the onset of high-Reynolds-number grid-generated wind tunnel turbulence. *J. Fluid Mech.* **320**, 331–368.

Nagib, H.M. & Chauhan, K.A. 2008 Variations of von Kármán coefficient in canonical flows. *Phys. Fluids* **20**, 101518.

Nickels, T.B., Marusic, I., Hafez, S.M. & Chong, M.S. 2005 Evidence of the k^{-1} law in a high-reynolds-number turbulent boundary layer. *Phis. Rev. Lett.* **95**, 074501.

Orlandi, P. 1997 Helicity fluctuations and turbulent energy production in rotating and non-rotating pipes. *Phys. Fluids* **9**, 2045–2056.

Orlandi, P. 2000 *Fluid flow phenomena: a numerical toolkit*. Kluwer.

Perry, A.E. & Abell, C.J. 1977 Asymptotic similarity of turbulence structures in smooth-and rough-walled pipes. *J. Fluid Mech.* **79**, 785–799.

Perry, A. E. & Li, J.D. 1990 Experimental support for the attached-eddy hypothesis in zero-pressure-gradient turbulent boundary layers. *J. Fluid Mech.* **218**, 405–438.

Pirozzoli, S. & Bernardini, M. 2013 Probing high-Reynolds-number effects in numerical boundary layers. *Phys. Fluids* **25**, 021704.

Pope, S.B. 2000 *Turbulent flows*. Cambridge University Press.

Rogers, M.M. & Moin, P. 1987 The structure of the vorticity field in homogeneous turbulent flows. *J. Fluid Mech.* **176**, 33–66.

Saddoughi, S.G. & Veeravalli, S.V. 1994 Local isotropy in turbulent boundary layers at high Reynolds number. *J. Fluid Mech.* **268**, 333-372.

Schultz, M.P. & Flack, K.A. 2013 Reynolds-number scaling of turbulent channel flow. *Phys. Fluids* **25**, 025104.

Sillero, J., Jiménez, J. & Moser, R. D. 2013 One-point statistics for turbulent wall-bounded flows at Reynolds numbers up to $\delta^+ \approx 2000$. *Phys. Fluids* **25** (105102).

Simens, M.P., Jiménez, J., Hoyas, S. & Mizuno, Y. 2009 A high-resolution code for a turbulent boundary layers. *J. Comput. Phys.* **228**, 4218–4231.

Smith, C.R. & Metzler, S.P. 1983 The characteristics of low-speed streaks in the near-wall region of a turbulent boundary layer. *J. Fluid Mech.* **129**, 27–54.

Townsend, A.A. 1961 Equilibrium layers and wall turbulence. *J. Fluid Mech.* **11**, 97–120.

Townsend, A.A. 1976 *The Structure of Turbulent Shear Flow*. 2nd edn. Cambridge University Press.

Wu, X. & Moin, P. 2008 A direct numerical simulation study on the mean velocity characteristics in turbulent pipe flow. *J. Fluid Mech.* **608**, 81–112.